PNAS
www.pnas.org

Supplementary Information for

Absorption by water increases fluorescence image contrast of biological tissue in the shortwave infrared

Jessica A. Carr†, Marianne Aellen†, Daniel Franke, Peter T.C. So, Oliver T. Bruns*, Moungi G. Bawendi*

*Moungi G. Bawendi, E-mail: mgb@mit.edu
Oliver T. Bruns, E-mail: oliver.bruns@helmholtz-muenchen.de
† these authors contributed equally

This PDF file includes:

www.pnas.org/cgi/doi/10.1073/pnas.1803210115

Supplementary Information text

SWIR fluorescence imaging set-up. A fluorescence imaging set-up was assembled as previously described in detail.(1, 2) Briefly, the output of a 10 W 808 nm laser (Opto Engine; MLL-N-808) was coupled into a fiber (Thorlabs; MHP910L02) and passed through a ground-glass plate (Thorlabs; DG10-220-MD) directed over the working area. The final laser intensity at the working surface is approximately 50–70 mW/cm^2. Emitted light was directed off of a 1" silver elliptical mirror (Thorlabs; PFE10-P01) to an InGaAs camera (Princeton Instruments; NIRvana, 640x512 pixel array) equipped with achromatic doublet lenses (Thorlabs; AC254-150-C and AC254-75-C; depth of field approximately 1.5 mm). The laser light was blocked with two colored glass 2" 850 nm longpass filters (Thorlabs; FGL850S) in front of the lenses and an 850 nm longpass dielectric filter (Thorlabs; FELH0850) in front of the sensor. Emission light was selected using various 50 nm bandpass filters (Edmund Optics) between the lenses.

All images were background-corrected using LightField software and analyzed using ImageJ. The camera was set to High Gain, cooled to -80ºC, and the analog to digital conversion rate was chosen to be either 2 MHz (for capillary phantom images and *ex vivo* tissue images) or 10 MHz (for *in vivo* images). Other acquisition settings (e.g. integration time, filters) for each figure are detailed in **Table S1**. The integration times were chosen to obtain approximately the same intensity value (around 10,000 average counts) for each image, such that the ratio of signal to camera noise (read and dark noise) could be approximately maximized while keeping the maximum intensity pixels within the limit of linear detection (i.e. sufficiently below saturation). In addition, to minimize the contribution of dark noise in images with long integration times, frame-averaging over 10 consecutive frames was performed for all wavelength bands. To confirm that camera noise and integration time have negligible effects on our contrast calculations, we calculated the average pixel intensity of the 10 frame average of background-subtracted dark images at each of the integration times used for the *in vivo* imaging data-set. We found dark images to have on average 0.01-0.2% of the counts of an *in vivo* brain vasculature image with the same integration time. The average dark image counts were 0.1-1% of the *in vivo* image standard deviations. Thus, the contrast of our images is primarily photon-noise-limited, such that signal as well as background intensity both scale linearly with integration time and consequently any ratio of two intensities is not affected by the integration time.

Intralipid tissue phantom preparation and imaging. Tissue phantoms were designed based on previous literature which confirmed similarity to biological tissue optical properties.(3–8) Intralipid® 20% (Baxter Healthcare Corporation), as a scattering medium, was diluted to 1% in water (H_2O) to mimic the attenuation of tissue, or in deuterium oxide (D_2O, Aldrich; 99.9 atom % D) which exhibits approximately equal scattering properties but has no absorption in the SWIR. Attenuation spectra of the phantom materials were recorded on a Cary 5000 UV-Vis-NIR infrared spectrometer from Varian (**Fig. S1A**).

Lead sulfide (PbS) quantum dots (QDs) were prepared according to the procedure of Hines and Scholes, and solutions with emission maxima near 1020 nm, 1200 nm, and 1430 nm were mixed to obtain a broadband SWIR emitter.(9) Photoluminescence spectra of the quantum dot mixture (**Fig. S1B**) was measured by exciting the samples with a 532 nm diode laser, and collecting the emission using a pair of gold-coated off-axis parabolic mirrors directing to a single-grating

spectrometer (Acton; Spectra Pro 300i). The output of the spectrometer was measured using a liquid nitrogen cooled InGaAs line camera (Princeton Instruments; OMA V, 512×1 pixel array).

Glass capillaries (approximately 1 mm outer diameter, 5 μL calibrated pipets, VWR, Cat No. 53432-706) were filled with the PbS mixture and submerged in the liquid phantoms individually or in two, perpendicular layers. Submersion depths of 2 mm and 4 mm were chosen for the two-layer capillaries to mimic overlapping vessels beneath a layer of tissue; the depth roughly corresponds to that reported previously for brain vessels underlying the scalp tissue of a mouse.(10) The phantom was placed in the imaging set-up described above (**Fig. 1C**) and images were acquired for different wavelengths across the SWIR (**Fig. S1D**). The images were used to derive the plot shown in **Fig. 1**, and a line of interest across a single capillary was used to assess capillary resolution (**Fig. S2**).

Contrast quantification. We quantified image contrast using the coefficient of variation, which is defined as the ratio of the standard deviation in signal intensities, σ, to the mean signal intensity, μ,

$$c_V = \frac{\sigma}{\mu}. \quad (1)$$

In a high contrast image, pixel intensities are high for regions of signal and are low for regions of background, resulting in a high σ and thus in a high value of the contrast metric. Low contrast images, on the other hand, have little variability in pixel intensity, and thus a low σ and contrast metric. Given that we want to assess the contrast for a local feature within a larger normalized image, we further divide σ by μ to account for the fact that a small σ is negligible if the average intensity within the region of interest is high, while the same small σ matters if the average intensity is low. This metric is applicable when comparing different images of the same object, and can be applied to a single feature of interest or an entire image containing multiple features. Throughout this study, c_V has only been compared among images containing the same objects. As c_V can be strongly affected by the relative size of bright objects in an image, it is important to note that the absolute values of c_V cannot be used for a global comparison of images of different structures.

We have considered using other metrics, such as the signal to noise ratio (SNR), the contrast to noise ratio (CNR), the signal to background ratio, and the Weber fraction to quantify image quality. However, these metrics require a region of interest with a clearly defined object of interest with known boundaries between the signal-generating feature and the background.(11) In the case of our *in vivo* and *ex vivo* tissue images, the "signal" and "background" portions of a feature's intensity profile are difficult and somewhat subjective to assign, thus we prefer to use c_V as our main contrast metric throughout the text, as this metric does not require such a subjective determination. Despite this, we include below a comparison of c_V to these other metrics for one feature of interest in our *in vivo* image dataset, and show reasonable agreement (see **Brain vasculature imaging *in vivo* with a quantum dot mixture** section).

Weakly-scattering tissue phantom based on silica beads. We reproduced the contrast trend observed in our Intralipid-based phantoms in a separate tissue phantom based on silica beads as a scattering medium (**Fig. S3**). The polydisperse silica beads (U.S. Silica; MIN-U-SIL® 40) were dispersed at a concentration of 5 mg/mL in water to mimic the absorption of tissue, or dispersed in deuterium oxide which has no absorption in the SWIR. MIN-U-SIL® 40 contains ground silica beads with a median diameter of 11 μm and a maximum diameter of 40 μm. This size regime

mimics the size range of refractive objects in tissue, such as sub-cellular organelles (<10 μm), microvasculature (5–10 μm), and entire cells (10–50 μm).(3) The resulting phantom was weakly-scattering, approximating the scattering of tissue such as skull.(12–14). The D_2O phantom was used to measure the influence of scattering alone (without any absorption), while the H_2O phantom revealed the influence of scattering in the presence of absorption. The medium was stirred with a magnetic stir bar to prevent sedimentation of the silica beads while images were acquired across SWIR wavelengths.

We evaluated the contrast c_V [**Eq. (1)**] between the top capillary, which represents the object of interest, and the bottom capillary, which introduces a background signal. The contrast was observed to be relatively constant across SWIR wavelengths in the D_2O phantom. However, when D_2O in the phantom is replaced by water, contrast increases through 1450 nm and then decreases again up to 1600 nm, indicating an important role of absorption in the enhancement of contrast, as observed in our Intralipid phantoms.

Scattered photon trajectory length and intensity predicted by diffusion theory. We estimated the trajectory length and intensity of detected scattered photons with an analytical expression for diffusive photon transport across a slab of the Intralipid phantom medium. Commonly, Monte Carlo models are applied to simulate light propagation in tissue,(15–19) as well as diffusion theory that is in good agreement with Monte Carlo models and experimental results.(20, 21) Here, we evaluate the temporal profile of photons exiting a slab of a scattering and absorbing medium as predicted by diffusion theory and described in reference (21). The scattering length is approximated by the attenuation spectrum of Intralipid diluted to 1% in D_2O (**Fig. 1**), assuming that the absorption of D_2O in the wavelength range from 900 nm to 1600 nm is negligible compared to the scattering. The absorption length is extracted from the attenuation spectrum of pure D_2O and water. For the transport mean free path, we take the inverse of the sum of the scattering and the absorption coefficients. All wavelength-dependent coefficients are averaged over 50 nm to imitate the bandpass filters used in the phantom experiments. The slab width is taken to be 2 mm which is the immersion depth of the single capillary in our experiment. We transform the temporal distribution to a distribution of trajectory lengths by multiplying the time with the speed of light.

For the D_2O phantom, it is obvious that the trajectory length distribution for the bandpass filters centered at 1350 nm and 1450 nm are hardly distinguishable (**Fig. S4A**). This is a result of little difference in the scattering and the absorption coefficient between 1350 nm and 1450 nm, hence the similarity in the trajectory lengths of the scattered photons. In contrast, the water phantom trajectory distribution maximum is ten times shorter for the 1450 nm photons compared to 1350 nm photons, due to a strong increase in the absorption between 1350 nm and 1450 nm, which decreases the chance for photons with long path lengths to arrive at the detector. The peak trajectory length at 1450 nm is decreased by a factor of fifty between the D_2O and the water 1% Intralipid medium, illustrating that photons with long path lengths are being absorbed and thus cannot reach the detector.

The intensity of scattered and ballistic photons arriving at the detector is evaluated with expressions from reference (21). We estimate the solid angle of collection for our SWIR fluorescence imaging set-up to be about 0.1% of a full sphere. Absorption and scattering coefficients are taken from experimental data as described above. In addition to a 1% Intralipid emulsion, a 10% Intralipid emulsion is modeled using scattering coefficients obtained from Mie

theory.(22) For 1% Intralipid in water at a depth of 2 mm, the ballistic photons outweigh scattered photons (**Fig. S4B**). This is in accordance with the single capillary images, where the capillary boundaries are clearly distinguishable for all SWIR wavelengths (**Fig. S2**). In the water absorption peak at 1450 nm, the intensity of both scattered and ballistic photons decreases drastically. However, the scattered photons are stronger affected by the absorption than the ballistic photons, resulting in the intensity ratio of ballistic to scattered photons being greatest at 1450 nm (**Fig. S4C**). The high intensity ratio yields the high contrast observed in the single capillary images (**Fig. S2**). To illustrate the capabilities of scattering suppression at SWIR wavelengths we predict the scattered and ballistic photon intensity for a medium with 10% Intralipid in water. The ballistic photons are strongly attenuated at short wavelengths as they undergo scattering, thus scattered photons dominate (**Fig. S4B**). The increasing strength of water absorption elevates the intensity ratio above one for wavelengths longer than 1400 nm (**Fig. S4C**). The maximum intensity ratio occurs at 1450 nm and is more than fifty times greater than the intensity ratio at 1600 nm, where scattering is the smallest for the plotted wavelengths.

The diffusion transport model neatly describes how scattering is affected by absorption in our single capillary phantom. It points out how the distribution of trajectory lengths of scattered photons are shifted to shorter path lengths, as photons with long trajectories are likely to be absorbed. The intensity of scattered photons is strongly decreased at wavelengths where absorption is strong, allowing for a high ratio of ballistic to scattered photons. Even for a highly scattering medium with a considerably decreased amount of ballistic photons, such as 10% Intralipid in water, the absorption can lift the intensity of ballistic photons over that of scattered photons. In addition, the model illustrates how the increase in the intensity ratio of ballistic photons over scattered photons comes at the cost of total intensity.

Brain vasculature imaging *in vivo* with a quantum dot mixture. All animal experiments were conducted in accordance with approved institutional protocols of the MIT Committee on Animal Care. Indium arsenide (InAs)-based (InAsCdSeCdS and InAsCdSeZnS core-shell-shell) QDs were synthesized(1) and transferred into aqueous solution via phospholipid micelles(23) as previously described. To obtain broadband SWIR emission, QD samples in aqueous solution emitting at 970 nm, 1110 nm, and 1300 nm were mixed. A C57BL/6J mouse (34 g, male, 22 weeks, Jackson Lab) was anaesthetized, shaved, and placed in the imaging setup described above. The mouse was irradiated with 808 nm laser light at 50-70 mW/cm^2 and 300 μg of aqueous QD-phospholipid micelles were injected via the tail vein. The irradiation power used in this study is well below the limit recommended by the American National Standards Institute (ANSI) for Safe Use of Lasers, which is a flux of 330 mW/cm^2 for 808 nm continuous wave light. The brain vasculature was imaged using 50 nm bandwidth bandpass filters centered across SWIR wavelengths, optimizing the focus of the central brain feature after each filter change (**Fig. S5**). The images were used to calculate contrast as plotted in **Fig. 2**, **Fig. S6**, and **Fig. S10**.

We defined a region of interest across one vessel in the brain and investigated the contrast using our primary contrast metric c_V [**Eq. (1)**] and other common metrics of contrast or image quality, including the CNR, the signal to background ratio, and the Weber fraction. We considered using the SNR, defined as the ratio of the average signal intensity to the standard deviation of the background intensities, however, in the case of significant bias in an image, as from haze, or in our case, scattering, the SNR metric fails to accurately reflect image contrast.(24) In these cases, the

signal intensity is high and the background standard deviation is low, yielding a high SNR, but the background intensity is also high in these images, resulting in poor contrast. Furthermore, the background is not uniform in the image in its entirety, and cannot be subtracted from the image to improve contrast. We believe that the CNR or c_V are more appropriate metrics in these scenarios.(25) To calculate the CNR [**Eq. (2)**], one first finds the amplitude of the signal, defined as the absolute difference between the signal peak (I_{max}) and the baseline of the signal (μ_{bg}) before dividing by the standard deviation of the background intensities (σ_{bg}):

$$\mathrm{CNR} = \frac{I_{max} - \mu_{bg}}{\sigma_{bg}}. \quad (2)$$

The use of signal amplitude in this metric thus takes into consideration the effect of bias in the images. We also calculated the signal to background ratio [**Eq. (3)**], defined as the mean signal intensity of the object of interest divided by the mean intensity of all other values in the region of interest which compose the background signal:

$$\frac{\mu}{\mu_{bg}}. \quad (3)$$

Finally, we also calculated the Weber fraction [**Eq. (4)**] of our region of interest, defined as

$$\frac{\mu - \mu_{bg}}{\mu_{bg}}. \quad (4)$$

Plotting these three contrast metrics against bandpass center wavelength shows good agreement with the water absorptance spectrum (**Fig. S6B**) and with the contrast metric, c_V (shown in **Fig. 2**). We further assessed the contrast metric c_V [**Eq. (1)**] for regions of interest across two additional vessels in the brain, and for all pixels of the image (**Fig. S6C-E**). In all cases, the trends were in good agreement with the water absorptance spectrum and with each other.

Measurement of contrast, resolution, and penetration depth in *ex vivo* tissue microscopy. For microscopy imaging, a QD emulsion was prepared by adding 1 mg of InAs-based QDs(1) with peak emission near 1150 nm and 1420 nm (**Fig. S7A**) dispersed in chloroform to a mixture of 28 μL lecithin (phosphatidylcholine, 25 mg/mL in chloroform), 100 μL of phospholipid-PEG2000 (25 mg/mL in chloroform, Avanti Polar Lipids; Cat. No 880130), and 400 μL of soybean oil (25 mg/mL in chloroform). The mixture was sonicated for 30 seconds, and afterwards the remaining solvent was evaporated by pressurized air flow. Particles were re-dispersed in 2 mL of 0.9% sodium chloride (USB; Bacteriostatic 0.9% Sodium Chloride Injection) and the mixture was sonicated until a homogenous emulsion was formed. The final solution was filtered through a 0.45 μm pore filter after sonication and again immediately before injection.

Two hundred microliters of the QD emulsion was injected intravenously via the tail vein into a C57BL/6J mouse (The Jackson Laboratory, male, 9 weeks old). It is known that these QD emulsion particles are taken up by the Kupffer cells in the liver.(26) Approximately 20 minutes after emulsion administration, a perfusion fixation was performed using 2% paraformaldehyde (PFA, Electron Microscopy Sciences, EM grade, 20% solution) in phosphate-buffered saline (PBS, Corning, PBS 1X), and the liver was dissected. For imaging, the liver sample was kept in a glass-bottom micro-well dish (MatTek Corporation) containing water (Corning; Cell Culture Grade Water) to avoid dehydration. The micro-well dish was placed on the stage of a microscope to acquire z-stacks of images for different wavelengths (**Fig. S7B-C**). The 808 nm laser output of the multimode fiber was directed through the diffuser of a laser speckle reducer (Optotune; LSR-3005)

and deflected at a silver mirror (Newport; 10D20ER.2) after which it entered an inverted microscope (Nikon; Eclipse Ti) through its backport unit. A longpass 900 nm dichroic mirror (Thorlabs; DMLP900R) guided the laser light onto the back aperture of the objective (Nikon; CFI Plan Apochromat λ 10x or 20x) which focused the laser onto the sample placed on a motorized stage (Ludl Electronic Products Ltd.; MAC 6000 Systems). The 10x objective with NA 0.45 has a theoretical depth of field between 9-12 μm for wavelengths between 1000 and 1600 nm (with greater depth of field for longer wavelengths) and the 20x objective with NA 0.75 has a theoretical depth of field between 3-4 μm which are in reasonable agreement with our experimentally observed values. The objective was calibrated for chromatic aberrations in the z-direction. Light emitted by the sample was collected by the same objective and passed through a longpass 900 nm dichroic mirror (Thorlabs; DMLP900R), a hard-coated 850 nm longpass filter (Thorlabs; FELH0850), and a 50 nm bandpass filter (Edmund Optics) for wavelength-selective imaging. The light was directed to an output port of the microscope onto the array of an InGaAs camera (Princeton Instruments; NIRvana, 640x512 pixel array). All images were background-corrected using NIS-Elements software and analyzed using MATLAB®. The camera was set to High Gain, cooled to -80°C, and the analog to digital conversion rate was set to 2 MHz. Other acquisition settings (e.g. integration time, filters) for each figure are detailed in **Table S1**.

The penetration depth at different wavelength bands for the liver tissue sample was evaluated with an adapted image processing algorithm from Rowlands et al.(27) in MATLAB® R2016a. Each image of the z-stack was transformed to Fourier space, applying a two-dimensional fast Fourier transform. The amplitude spectrum was calculated and divided by the total number of pixels for image size normalization. The quadrants were shifted such that low frequencies were displayed in the center and high frequencies at the edges of the Fourier space image. Radial averaging was performed over a ring of one pixel thickness centered at the DC frequency. This averaging process is repeated for all ring radii ranging from the DC frequency (center pixel) to the Nyquist frequency (edge pixel). The radial averaging resulted in the intensity of all spatial frequencies.

A threshold that determines the highest visible frequency in a single image was found by fitting the logarithm of the frequency intensity versus spatial frequency curve with an exponential function of the form $f(x) = a \cdot e^{-bx} + c$. The median of the parameter c, which represents the noise baseline of the camera, was determined over all images of one z-stack and averaged over all z-stacks. The highest visible frequency was set at the highest frequency that had greater intensity than twice the overall noise baseline, corresponding to a signal to noise ratio of 2. It was found that a signal to noise ratio of 2 yields penetration depths that agree best with a viewer's perception when looking at a random choice of z-stacks. The frequency thresholding procedure was repeated for all images of one z-stack, resulting in a threshold frequency versus imaging depth curve. A five-point moving average was applied on this curve to reduce the influence of outliers, and create a continuous threshold frequency curve.

To extract the penetration depth, the threshold frequency for a given imaging depth was compared to the spatial frequency of the cells, which was approximated by 100 lp/mm, as cells have an average size of roughly 10 μm and are homogeneously distributed. The penetration depth was defined at the imaging depth where the threshold frequency drops below the spatial frequency of the cells. This procedure was performed for z-stacks acquired at different wavelength bands of the SWIR in order to determine the penetration depth as a function of wavelength.

We show the increase in contrast and penetration depth with increasing attenuation across SWIR wavelengths in **Fig. 3**, and here, show that this results in improved imaging resolution. We define resolution as the minimum distance between two distinguishable features in an image. At a depth of 58 μm in the liver tissue, we see that two nearby cells cannot be resolved by an intensity profile across the cells while imaging with 1000 nm and 1200 nm BP filters; however, these cells are resolvable as two distinct structures while using longer 1450 nm and 1600 nm BP filters (**Fig. S8**). Of note, the imaging performed in this study is not at the diffraction limit, which in the case of sufficient imaging contrast would cause decreasing resolution with increasing wavelength. The resolution limits described in this paper mainly originate from the poor contrast of wavelength channels with relatively low tissue absorption.

Theoretical contrast model for understanding penetration depth trends. We developed a basic theoretical model to assess fluorescence imaging contrast and penetration depth in tissue. In our model, tissue is described by a semi-infinite slab with emitting cells homogenously distributed throughout the slab. The signal of interest, *S*, arises from the focal plane at depth *D*, and background signal, *BG*, arises from all planes elsewhere (see schematic in **Fig. 4A**). The signal intensities are modeled according to Beer-Lambert's law, resulting in

$$\begin{aligned} S &= S_0 \cdot e^{-D\cdot\mu_{ex}} \cdot e^{-D\cdot\mu_{em}} \\ &= S_0 \cdot e^{-D(\mu_{ex}+\mu_{em})}. \end{aligned} \tag{5}$$

Here, S_0 describes the in-focus signal intensity at zero depth, and μ_{ex} and μ_{em} are the attenuation coefficients of the excitation and emission wavelengths, respectively. We consider the attenuation coefficient as a lumped parameter containing all sources of attenuation (e.g. absorption and scattering). The first exponential term accounts for the attenuation of the excitation light on the way to the focal plane and the second exponential term denotes the decay of the emitted light traveling from the focal plane to the detector.

Similarly, we calculate the background intensity, assuming that the emission intensity (before the effect of attenuation) is uniform through all planes of the slab and finding the sum:

$$\begin{aligned} BG &= BG_0' \cdot \int_0^\infty e^{-z(\mu_{ex}+\mu_{em})}\, dz \\ &= BG_0' \cdot \frac{1}{\mu_{ex}+\mu_{em}} \end{aligned} \tag{6}$$

where BG_0' is the out-of-focus background intensity per millimeter slab at zero depth. The contrast was then calculated by the ratio of signal and background:

$$C = \frac{S_0}{BG_0'} \cdot e^{-D(\mu_{ex}+\mu_{em})} \cdot (\mu_{ex} + \mu_{em}) \tag{7}$$

and plotted as a function of the total attenuation at a fixed depth of 1 mm (**Fig. 4B**).

With this model, we estimated the penetration depth trend across SWIR wavelengths. The penetration depth can be thought of as the maximum imaging depth at which one can still resolve the structures of interest; this depth is reached when the image contrast drops below some threshold contrast value. In our model, we required *C* to be at least 3 such that S_0 is significantly greater than BG_0' at zero depth, and therefore distinguishable from background. We first calculated the contrast as a function of imaging depth (*D*) and background (BG_0') using literature values(14) for the tissue attenuation coefficient at 808 nm for the excitation wavelength and at wavelengths of different

SWIR bandpass filters for the emission (**Fig. S9**). Then, using the established threshold for *C*, we estimated the relative penetration depth for each wavelength as shown in **Fig. 5**.

Trade-off between signal intensity and image contrast. While we show here that imaging at wavelengths of greater attenuation can favor contrast and penetration depth in the SWIR, these benefits come at the cost of overall signal intensity. We show here that the signal intensity of the *in vivo* mouse brain vasculature images described above mirrors the trend in contrast (**Fig. S10**). We therefore suggest that in the case of limited signal (e.g. a weakly-emitting contrast agent, a small object of interest, or a deeply submerged structure) a compromise must be established to select a wavelength that provides sufficient signal intensity for detection above the detector noise, but with sufficient attenuation to resolve the structure of interest and optimize its contrast.

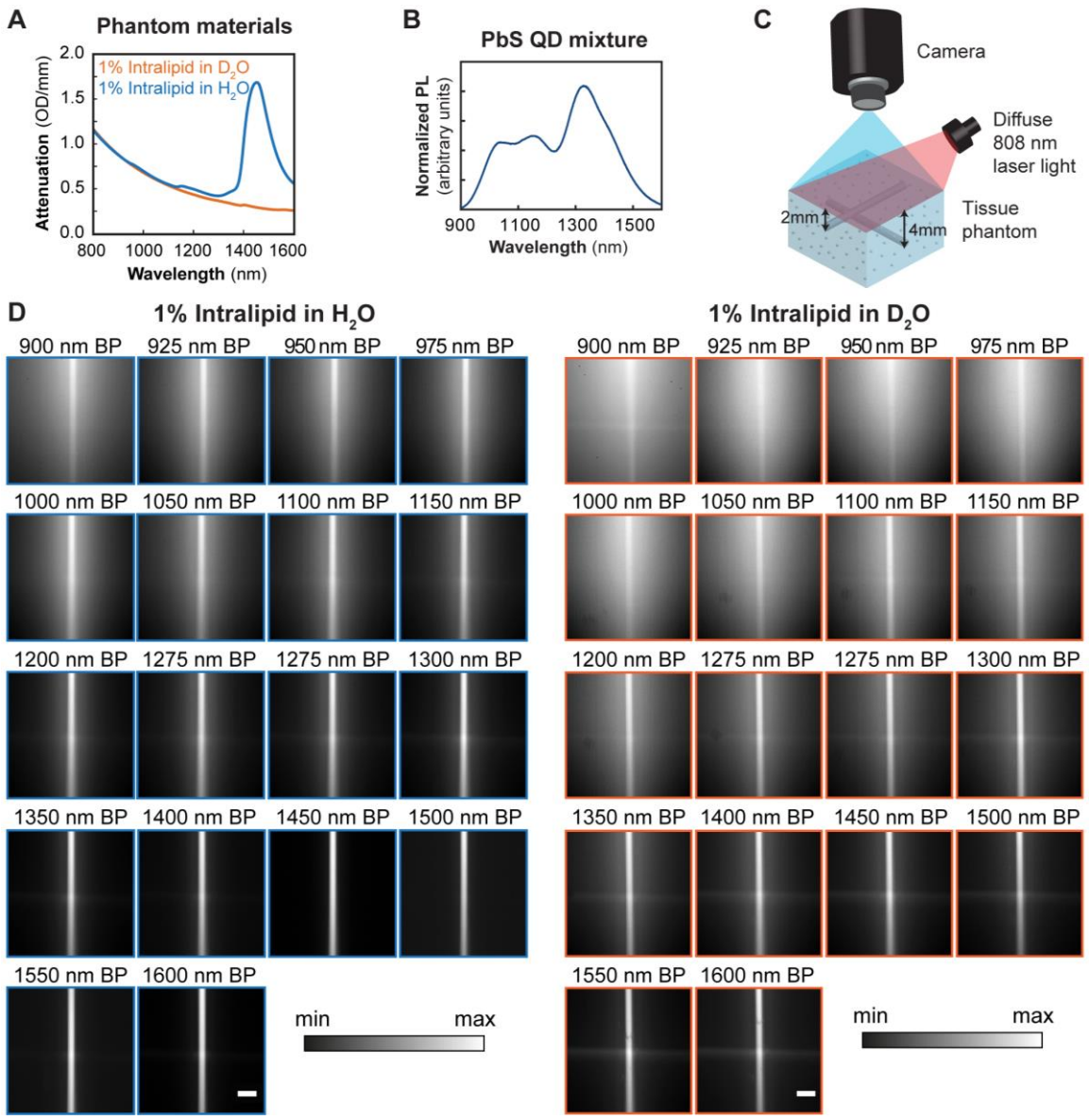

Fig. S1. Tissue phantom properties, imaging set-up, and complete set of two-layer capillary phantom images in 1% Intralipid. (**A**) The tissue phantom is composed of Intralipid® diluted to 1% in either water (H_2O, blue line) or deuterium oxide (D_2O, orange line). (**B**) We filled two capillaries with a mixture of SWIR-emitting lead sulfide (PbS) quantum dots, the photoluminescence (PL) spectrum of which shows broad SWIR emission. (**C**) We then submerged the capillaries in a perpendicular arrangement 2 mm and 4 mm deep in the liquid tissue phantom, illuminated with diffuse 808 nm light, and filtered the emission through 50 nm bandwidth bandpass filters centered across SWIR wavelengths before imaging from the top with an InGaAs SWIR camera. (**D**) We show the complete set of images here with blue outlines indicating water-based and orange outlines indicating deuterium oxide-based phantoms.

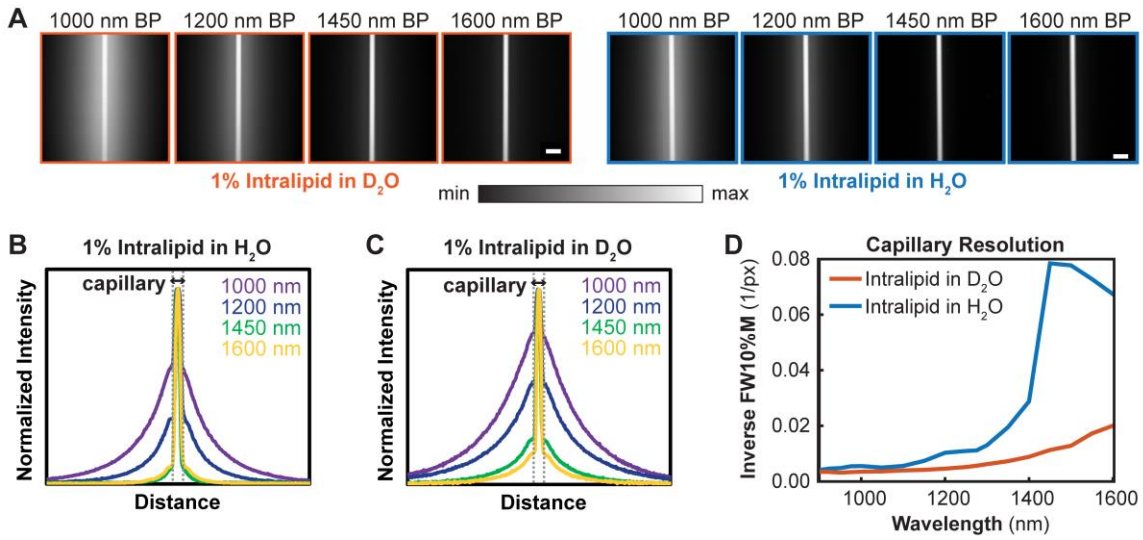

Fig. S2. Water absorption enhances contrast and resolution in a tissue phantom via scattering suppression. (**A**) Representative images of a SWIR-emissive capillary submerged 2 mm deep in a 1% Intralipid® phantom are shown illuminated with 808 nm light, and the emission filtered through 50 nm bandwidth bandpass filters centered at 1000 nm, 1200 nm, 1450 nm, and 1600 nm. Scale bars represent 1 mm and images are scaled to fill the maximum number of displayable intensities. (**B**) The intensity profile across the capillary immersed in the H_2O-based phantom shows narrowing of the scattering pedestal at wavelengths of stronger water absorption, and overall greater narrowing than (**C**) the scattering pedestal of capillaries immersed in the D_2O-based phantom which sharpens continuously. (**D**) The inverse of the full width at 10% maximum height (FW10%M) of the intensity profiles shows that the scattering pedestal of capillaries immersed in the H_2O-based phantom narrows at wavelengths of stronger water absorption, and is overall more narrow than the scattering pedestal of capillaries immersed in the D_2O-based phantom, which sharpens continuously.

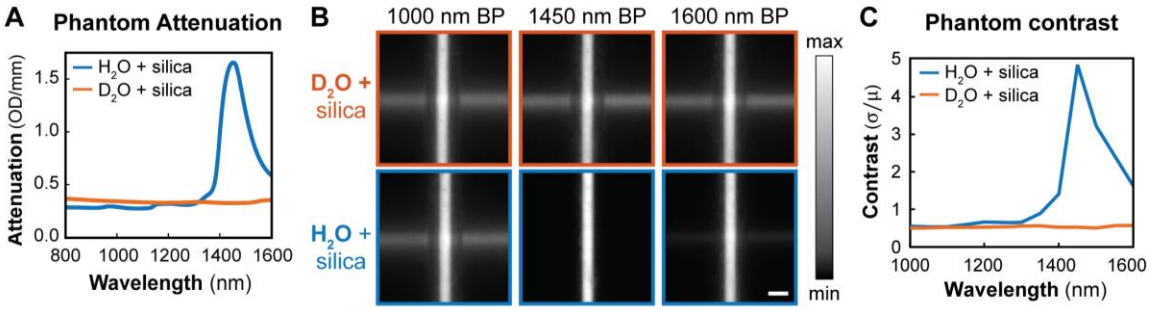

Fig. S3. Contrast trend in a weakly-scattering silica bead-based liquid tissue phantom. (**A**) The attenuation spectra of the H_2O-based silica phantom (blue) shows strong absorption and weak scattering while the D_2O-based phantom (orange) exhibits weak absorption and weak scattering. (**B**) Images of two SWIR-emitting capillaries submerged 1 mm and 3 mm deep in a D_2O-based (top row) and H_2O-based (bottom row) tissue phantom were taken with 50 nm bandwidth bandpass (BP) filters centered across the SWIR. Images are scaled to fill the maximum number of displayable intensities and the scale bar represents 1 mm. (**C**) Plotting the contrast versus wavelength for the capillary images shows that contrast improves sharply with phantom attenuation in the H_2O-based phantom (blue), while little change in the contrast is observed in the D_2O-based phantom (orange).

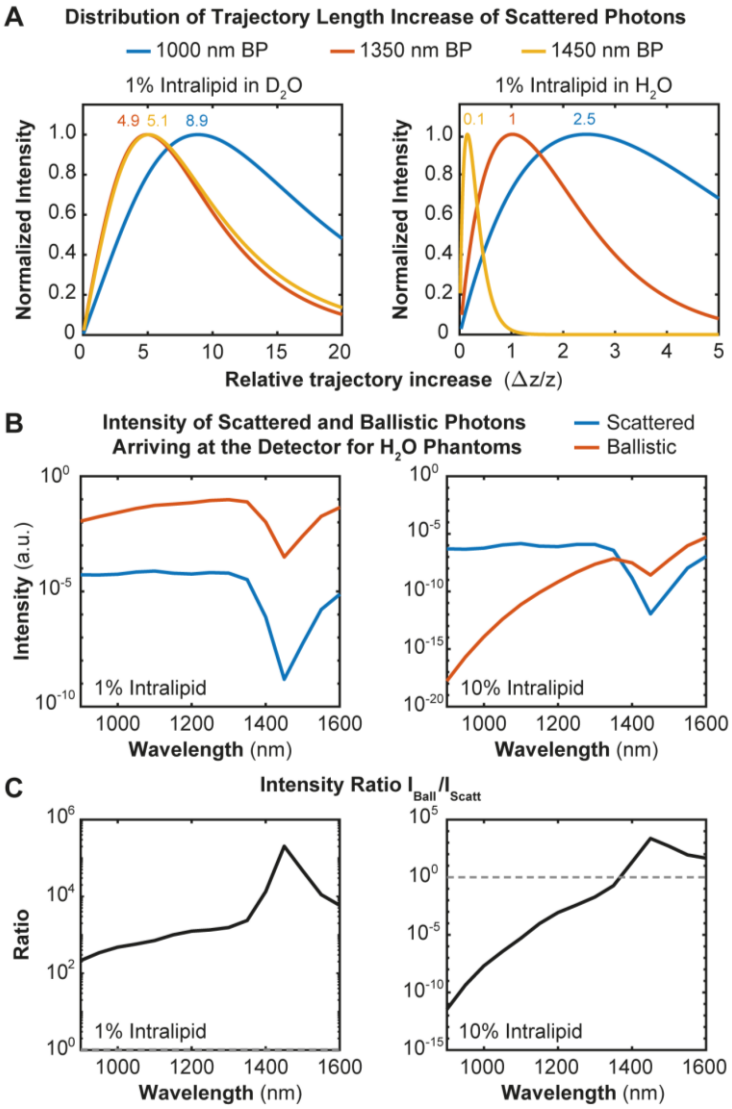

Fig. S4. Comparison of trajectory length and intensity of scattered and ballistic photons in a diffusive transport model. (**A**) Distribution of the increase of the trajectory length of scattered photons compared to the path length of ballistic photons normalized by the slab width of 2 mm. The curves represent emitted photons within a 50 nm bandwidth bandpass filter (BP) centered at 1000 nm, 1350 nm, and 1450 nm. The numbers indicate the relative trajectory increase at the intensity maximum of the distribution. (**B**) Comparison of the intensity of scattered and ballistic photons arriving at the detector as a function of wavelength. The intensities are plotted for a 1% and a 10% Intralipid® emulsion in water. The intensities are scaled to one photon. (**C**) The relative intensity ratio of the ballistic and scattered photons from (**B**). The grey dashed line indicates an intensity ratio of one.

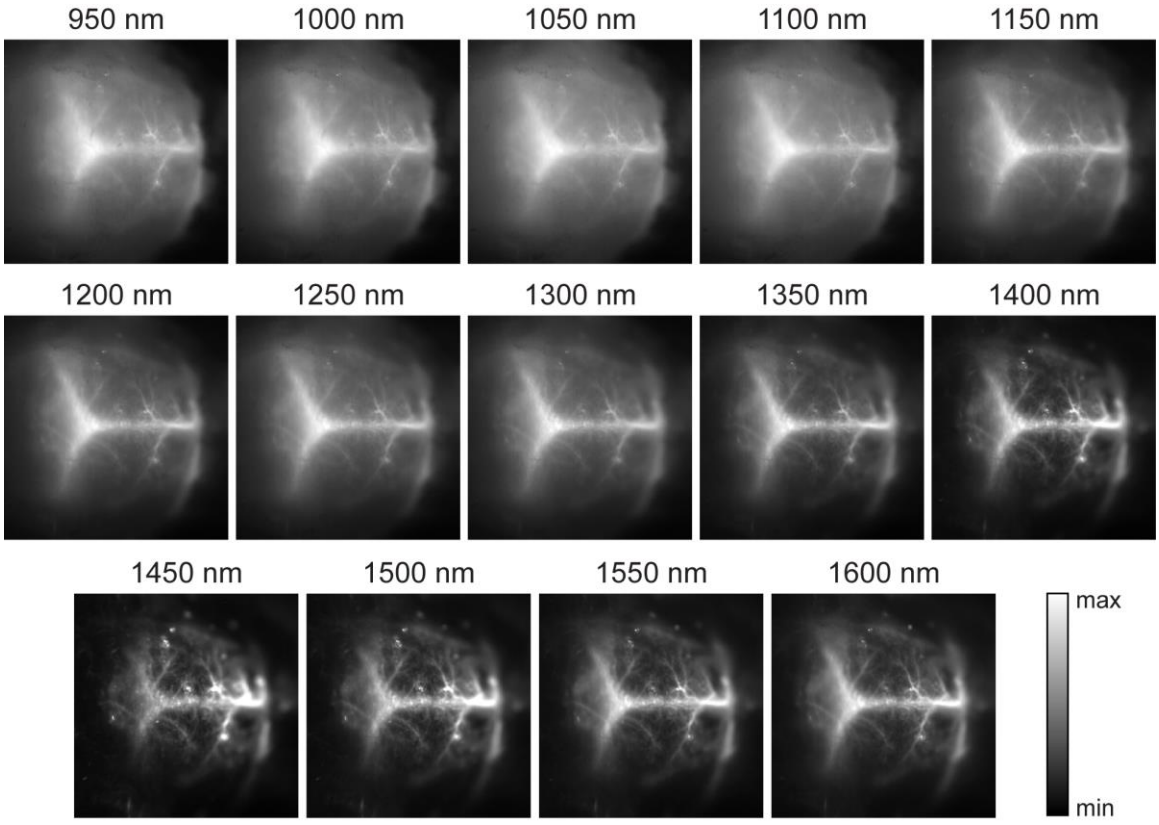

Fig. S5. Mouse brain vasculature imaged across SWIR wavelengths. The brain vasculature of a mouse was fluorescently labeled with a broadly-emitting InAs-based quantum dot mixture and imaged through approximately 1-2 mm of intact skin and skull.(10) The emission was filtered with 50 nm bandwidth bandpass filters centered in 50 nm spacing between 950 nm and 1600 nm. These images were used to generate the contrast versus wavelength plots in **Fig. 2**, **Fig. S6**, and **Fig. S10**, which show that the wavelength-dependence of contrast mimics the water absorptance spectrum.

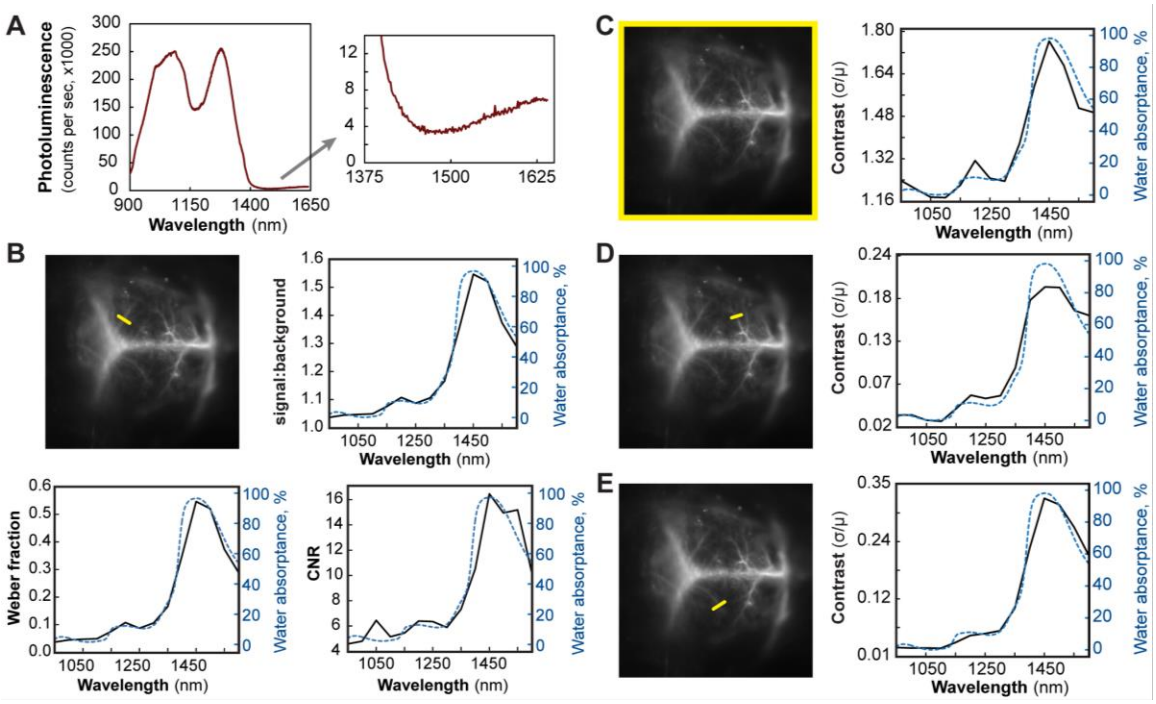

Fig. S6. Wavelength-dependence of contrast for different regions of interest and contrast metrics. We show the photoluminescence spectrum of the InAs-based QD mixture in aqueous solution used for noninvasive *in vivo* brain vasculature imaging of a mouse (**A**). We calculated the contrast for each of the images shown in **Fig. S5** using a line of interest (shown in yellow) across a particular vessel of interest with four different contrast metrics: c_V [**Eq. (1)**] as shown in **Fig. 2**, the signal to background ratio [**Eq. (3)**], the Weber fraction [**Eq. (4)**], and the contrast to noise ratio (CNR) [**Eq. (2)**]. The contrast was plotted against wavelength (black solid line) and overlaid with the water absorptance spectrum (%, blue dashed line) and shows good agreement (**B**). We further plotted the contrast c_V [**Eq. (1)**] using a region of interest containing the entire image (**C**) and across two additional brain vessels (**D**, **E**). Images shown are taken with a 1600 nm bandpass filter.

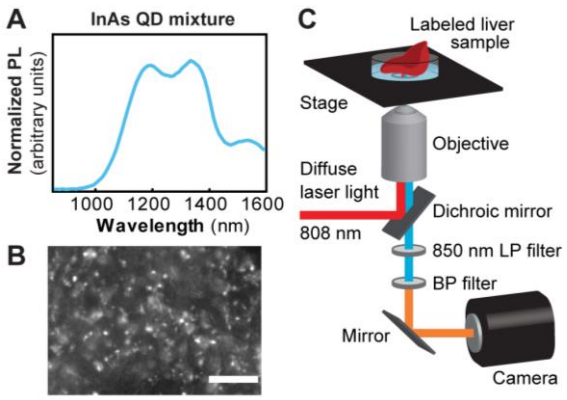

Fig. S7. *Ex vivo* liver microscopy. (**A**) The photoluminescence spectrum of an InAs-based quantum dot emulsion mixture shows broad SWIR emission. (**B**) The quantum dots accumulate in individual cells in the liver of a mouse, shown here imaged with a 50 nm bandpass filter centered at 1450 nm. The scale bar represents 100 μm. (**C**) The liver is imaged via fluorescence microscopy using 808 nm laser light for excitation and the emission filtered through 850 nm long pass filters and a 50 nm bandwidth SWIR bandpass (BP) filter.

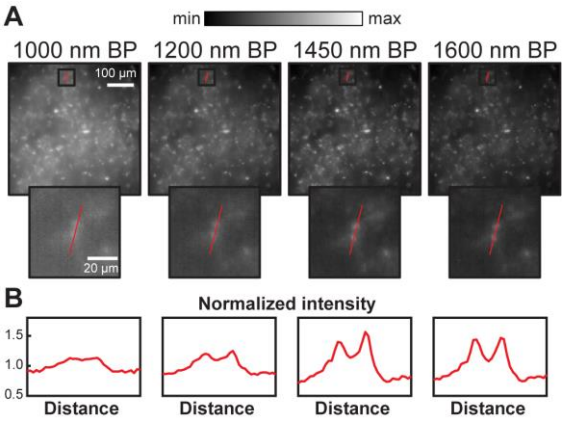

Fig. S8. Improvement of cell resolution in *ex vivo* tissue microscopy through wavelength selection. (**A**) Images of the QD-labeled liver tissue are shown taken at a depth of 58 μm at 20x magnification with bandpass (BP) filters centered at 1000 nm, 1200 nm, 1450 nm, and 1600 nm on an InGaAs camera. (**B**) The intensity plot for a line of interest shows that two nearby cells are best resolved at 1450 nm and 1600 nm.

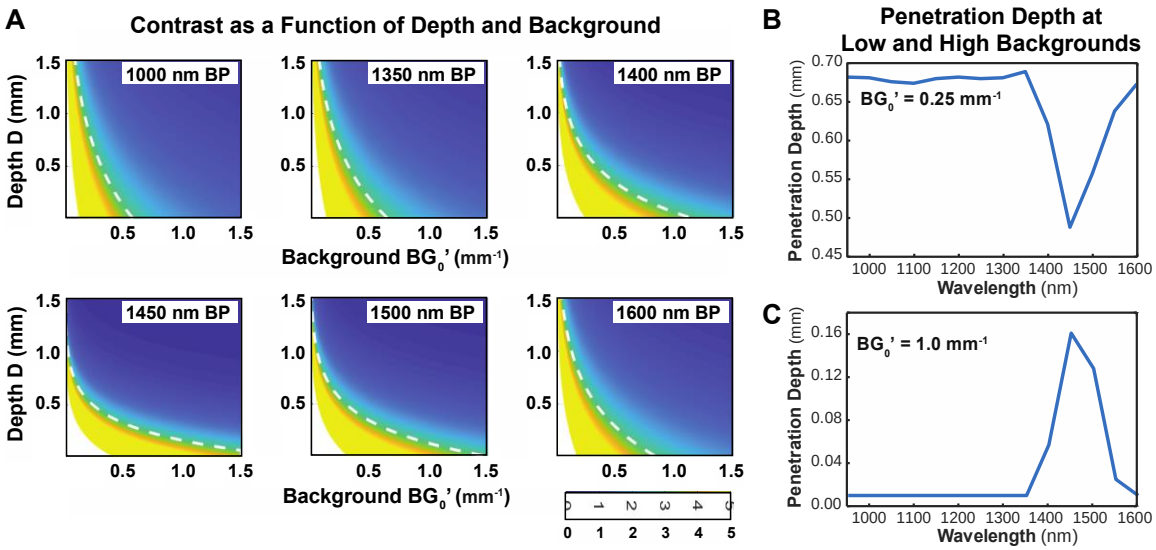

Fig. S9. Dependence of contrast on imaging depth and inherent background intensity. (**A**) Contrast is plotted as a function of imaging depth and inherent background intensity for a fixed level of signal. Contrast is scaled according to the color bar shown, with contrast values greater than 5 displayed at the maximum intensity color. The white dotted line indicates the threshold contrast value of three, considered to be the minimal resolvable contrast; values to the right of this line are considered unresolvable. Thus, this line indicates the maximum penetration depth for a given level of background signal in the system as plotted in **Fig. 5**. (**B**) The penetration depth shows opposing trends with SWIR wavelength for applications with low levels of background, versus (**C**) applications with high levels of background (schematized in **Fig. 5**).

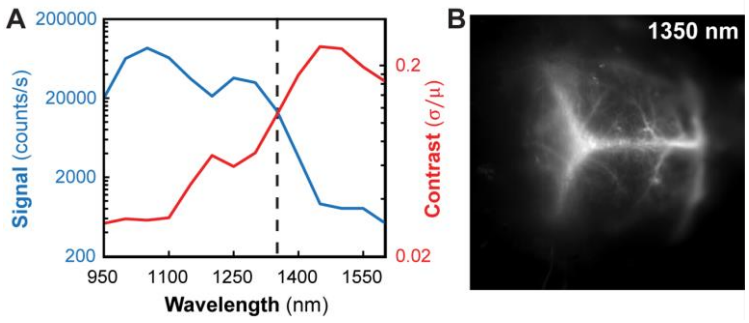

Fig. S10. Opposing wavelength dependencies of signal and contrast. (**A**) Absorption of water in tissue increases contrast, but at the cost of signal, shown here for *in vivo* brain vasculature fluorescence images described in **Fig. 2**. Wavelengths between 1200-1300 nm or beyond 1300 nm (as with a longpass filter) could be used to balance signal requirements and optimal contrast in applications with lower intensity signal insufficient for imaging at 1450 nm where contrast is maximized. The dashed line indicates the position of 1350 nm which is the center wavelength of the BP filter used to take the image shown in (**B**) requiring 200 ms integration time.

Table S1. The following table details the emission filters and exposure times used for each of the images presented. Filters are represented by a Thorlabs part number except for 50 nm bandwidth bandpass (BP) filters which are from Edmund Optics (EO).

Figure		Filters	Exposure Time (ms)	
Figure 1	B (1000 nm BP)	2xFGL1000S, FELH0850, 1000 nm BP (EO)	H_2O: 50	D_2O: 50
	B (1200 nm BP)	2xFGL1000S, FELH0850, 1200 nm BP (EO)	H_2O: 50	D_2O: 50
	B (1450 nm BP)	2xFGL1000S, FELH0850, 1450 nm BP (EO)	H_2O: 2500	D_2O: 50
	B (1600 nm BP)	2xFGL1000S, FELH0850, 1600 nm BP (EO)	H_2O: 1000	D_2O: 500
Figure S1	D (900 nm BP)	2xFGL1000S, FES1000, 900 nm BP (EO)	H_2O: 1000	D_2O: 2500
	D (925 nm BP)	2xFGL1000S, FES1000, 925 nm BP (EO)	H_2O: 250	D_2O: 500
	D (950 nm BP)	2xFGL1000S, FES1000, 950 nm BP (EO)	H_2O: 100	D_2O: 250
	D (975 nm BP)	2xFGL1000S, FES1000, 975 nm BP (EO)	H_2O: 50	D_2O: 100
	D (1000 nm BP)	2xFGL1000S, FELH0850, 1000 nm BP (EO)	H_2O: 50	D_2O: 50
	D (1050 nm BP)	2xFGL1000S, FELH0850, 1050 nm BP (EO)	H_2O: 25	D_2O: 50
	D (1100 nm BP)	2xFGL1000S, FELH0850, 1100 nm BP (EO)	H_2O: 25	D_2O: 50
	D (1150 nm BP)	2xFGL1000S, FELH0850, 1150 nm BP (EO)	H_2O: 25	D_2O: 50
	D (1200 nm BP)	2xFGL1000S, FELH0850, 1200 nm BP (EO)	H_2O: 25	D_2O: 50
	D (1250 nm BP)	2xFGL1000S, FELH0850, 1250 nm BP (EO)	H_2O: 50	D_2O: 50
	D (1275 nm BP)	2xFGL1000S, FELH0850, 1275 nm BP (EO)	H_2O: 25	D_2O: 25
	D (1300 nm BP)	2xFGL1000S, FELH0850, 1300 nm BP (EO)	H_2O: 25	D_2O: 25
	D (1350 nm BP)	2xFGL1000S, FELH0850, 1350 nm BP (EO)	H_2O: 25	D_2O: 25
	D (1400 nm BP)	2xFGL1000S, FELH0850, 1400 nm BP (EO)	H_2O: 100	D_2O: 50
	D (1450 nm BP)	2xFGL1000S, FELH0850, 1450 nm BP (EO)	H_2O: 2500	D_2O: 50
	D (1500 nm BP)	2xFGL1000S, FELH0850, 1500 nm BP (EO)	H_2O: 2500	D_2O: 100
	D (1550 nm BP)	2xFGL1000S, FELH0850, 1550 nm BP (EO)	H_2O: 1000	D_2O: 250
	D (1600 nm BP)	2xFGL1000S, FELH0850, 1600 nm BP (EO)	H_2O: 1000	D_2O: 500
Figure S2	A (1000 nm)	2xFGL1000S, FELH0850, 1000 nm BP (EO)	H_2O: 50	D_2O: 50
	A (1200 nm)	2xFGL1000S, FELH0850, 1200 nm BP (EO)	H_2O: 50	D_2O: 50
	A (1450 nm)	2xFGL1000S, FELH0850, 1450 nm BP (EO)	H_2O: 2500	D_2O: 25
	A (1600 nm)	2xFGL1000S, FELH0850, 1600 nm BP (EO)	H_2O: 1000	D_2O: 250
Figure 2	A (1000 nm)	2xFGL1000S, 1000 nm BP (EO)	50	
	A (1200 nm)	2xFGL1000S, 1200 nm BP (EO)	150	
	A (1450 nm)	2xFGL1000S, 1450 nm BP (EO)	2500	
	A (1600 nm)	2xFGL1000S, 1600 nm BP (EO)	5000	
Figure S3	B (1000 nm BP)	2xFGL1000S, 1000 nm BP (EO)	H_2O: 25	D_2O: 25
	B (1450 nm BP)	2xFGL1000S, 1450 nm BP (EO)	H_2O: 2000	D_2O: 10
	B (1600 nm BP)	2xFGL1000S, 1600 nm BP (EO)	H_2O: 1500	D_2O: 200
Figure 3	A (1000 nm BP)	DMLP900R, FELH0850, 1000 nm BP (EO)	200 for all depths	
	A (1200 nm BP)	DMLP900R, FELH0850, 1200 nm BP (EO)	180 for all depths	
	A (1450 nm BP)	DMLP900R, FELH0850, 1450 nm BP (EO)	2200 for all depths	
	A (1600 nm BP)	DMLP900R, FELH0850, 1600 nm BP (EO)	4000 for all depths	
Figure S5	950 nm	2xFGL1000S, FES1100, 950 nm BP (EO)	150	
	1000 nm	2xFGL1000S, FES1100, 1000 nm BP (EO)	50	
	1050 nm	2xFGL1000S, 1050 nm BP (EO)	50	
	1100 nm	2xFGL1000S, 110 nm BP (EO)	50	
	1150 nm	2xFGL1000S, 1150 nm BP (EO)	100	
	1200 nm	2xFGL1000S, 1200 nm BP (EO)	150	
	1250 nm	2xFGL1000S, 1250 nm BP (EO)	100	
	1300 nm	2xFGL1000S, 1300 nm BP (EO)	100	
	1350 nm	2xFGL1000S, 1350 nm BP (EO)	200	

	1400 nm	2xFGL1000S, 1400 nm BP (EO)	750
	1450 nm	2xFGL1000S, 1450 nm BP (EO)	2500
	1500 nm	2xFGL1000S, 1500 nm BP (EO)	2500
	1550 nm	2xFGL1000S, 1550 nm BP (EO)	2500
	1600 nm	2xFGL1000S, 1600 nm BP (EO)	5000
Figure S6	B, C, D, E	2xFGL1000S, 1600 nm BP (EO)	5000
Figure S8	A (1000 nm BP)	DMLP900R, FELH0850, 1000 nm BP (EO)	170
	A (1200 nm BP)	DMLP900R, FELH0850, 1200 nm BP (EO)	150
	A (1450 nm BP)	DMLP900R, FELH0850, 1450 nm BP (EO)	1200
	A (1600 nm BP)	DMLP900R, FELH0850, 1600 nm BP (EO)	2300
Figure S10	B	2xFGL1000S, 1350 nm BP (EO)	200

References

1. Franke D, et al. (2016) Continuous injection synthesis of indium arsenide quantum dots emissive in the short-wavelength infrared. *Nat Commun* 7:12749.
2. Bruns OT, et al. (2017) Next generation in vivo optical imaging with short-wave infrared quantum dots. *Nat Biomed Eng* 1:0056 EP.
3. Wang D, Chen Y, Liu JTC (2012) A liquid optical phantom with tissue-like heterogeneities for confocal microscopy. 3(12):3153–3160.
4. van Staveren HJ, Moes CJM, van Marle J, Prahl SA, van Gemert MJC (1991) Light scattering in Intralipid-10% in the wavelength range of 400-1100 nm. *Appl Opt* 30(31):4507–4514.
5. Driver I, Feather JW, King PR, Dawson JB (1989) The optical properties of aqueous suspensions of Intralipid, a fat emulsion. *Phys Med Biol* 34(12):1927–1930.
6. Flock ST, Jacques SL, Wilson BC, Star WM, van Gemert MJC (1992) Optical properties of intralipid: A phantom medium for light propagation studies. *Lasers Surg Med* 12(5):510–519.
7. Pogue BW, Patterson MS (2006) Review of tissue simulating phantoms for optical spectroscopy, imaging and dosimetry. *J Biomed Opt* 11(4):041102.
8. Lai P, Xu X, Wang L V (2014) Dependence of optical scattering from Intralipid in gelatin-gel based tissue-mimicking phantoms on mixing temperature and time. *J Biomed Opt* 19(3):35002.
9. Hines MA, Scholes GD (2003) Colloidal PbS Nanocrystals with Size-Tunable Near-Infrared Emission: Observation of Post-Synthesis Self-Narrowing of the Particle Size Distribution. *Adv Mater* 15(21):1844–1849.
10. Hong G, et al. (2014) Through-skull fluorescence imaging of the brain in a new near-infrared window. *Nat Photonics* 8(9):723–730.
11. Mora M, Tauber C, Batatia H (2005) Robust level set for heart cavities detection in ultrasound images. *Comput Cardiol* 32(4):235–238.
12. Bevilacqua F, Berger AJ, Cerussi AE, Jakubowski D, Tromberg BJ (2000) Broadband absorption spectroscopy in turbid media by combined frequency-domain and steady-state methods. *Appl Opt* 39(34):6498–6507.
13. Firbank M, Hiraoka M, Essenpreis M, Delpy DT (1993) Measurement of the optical properties of the skull in the wavelength range 650-950 nm. *Phys Med Biol* 38(4):503–510.
14. Jacques SL (2013) Optical Properties of Biological Tissues: A Review. *Phys Med Biol* 58(11):R37-61.
15. Wilson BC, Adam G (1983) A Monte Carlo model for the absorption and flux distributions of light in tissue. *Med Phys* 10(6):824–830.
16. Flock ST, Wilson BC, Patterson MS (1988) Hybrid Monte Carlo - Diffusion Theory Modelling Of Light Distributions In Tissue. ed Berns MW (International Society for Optics and Photonics), p 20.
17. Flock ST, Patterson MS, Wilson BC, Wyman DR (1989) Monte Carlo modeling of light propagation in highly scattering tissue--I: Model predictions and comparison with diffusion theory. *IEEE Trans Biomed Eng* 36(12):1162–8.
18. Prahl SA (1989) A Monte Carlo model of light propagation in tissue. eds Mueller GJ, Sliney DH, Potter RF (International Society for Optics and Photonics), p 1030509.
19. Wang L, Jacques SL, Zheng L (1995) MCML—Monte Carlo modeling of light transport in multi-layered tissues. *Comput Methods Programs Biomed* 47(2):131–146.
20. Lax M, Nayaranamurti V, Fulton RC (1988) Classical Diffusive Photon Transport in a Slab. *Laser Opt Condens Matter*:229–235.
21. Yoo KM, Liu F, Alfano RR (1991) Imaging through a scattering wall using absorption. *Opt Lett* 16(14):1068.
22. van Staveren HJ, Moes CJM, van Marie J, Prahl SA, van Gemert MJC (1991) Light scattering in lntralipid-10% in the wavelength range of 400–1100 nm. *Appl Opt* 30(31):4507.
23. Dubertret B, et al. (2002) In vivo imaging of quantum dots encapsulated in phospholipid micelles. *Science (80-)* 298(5599):1759–1762.
24. Jiang H, Lu N, Yao L (2016) A High-Fidelity Haze Removal Method Based on HOT for Visible Remote Sensing Images. *Remote Sens* 8(10):844.
25. Welvaert M, Rosseel Y (2013) On the Definition of Signal-To-Noise Ratio and Contrast-To-Noise Ratio for fMRI Data. *PLoS One* 8(11):e77089.
26. Heine M, et al. (2014) The cell-type specific uptake of polymer-coated or micelle-embedded QDs and SPIOs does not provoke an acute pro-inflammatory response in the liver. *Beilstein J*

Nanotechnol 5:1432–1440.
27. Rowlands CJ, Bruns OT, Bawendi MG, So PTC (2015) Objective, comparative assessment of the penetration depth of temporal-focusing microscopy for imaging various organs. *J Biomed Opt* 20(6):061107.